

# Study of a triple-discriminating plastic scintillator detector for fast neutrons, thermal neutrons, and $\gamma$ rays

---

**Y.H. Liu**,<sup>a,1</sup> **X.S. Zhang**,<sup>a</sup> **D.X. Lu**,<sup>a</sup> **W. Wang**,<sup>a,b,\*</sup> **G. Luo**,<sup>c,\*</sup> **F.P. An**,<sup>a,\*</sup>

<sup>a</sup>*School of Physics, Sun Yat-sen University,  
No.135 West Xingang Road, 510275 GuangZhou , China*

<sup>b</sup>*Institut Franco-Chinois de l'Énergie Nucléaire , Sun Yat-sen University,  
No. 2 Daxue Road,519082 Zhuhai, China*

<sup>c</sup>*School of Science, Sun Yat-sen University,  
No. 66 Gongchang Road, 518107 Shenzhen, China*

*E-mail:* [wangw223@mail.sysu.edu.cn](mailto:wangw223@mail.sysu.edu.cn), [anfp@mail.sysu.edu.cn](mailto:anfp@mail.sysu.edu.cn),  
[luog7@mail2.sysu.edu.cn](mailto:luog7@mail2.sysu.edu.cn)

**ABSTRACT:** Detecting fast and thermal neutrons plays a crucial role in neutrino experiments and reactor physics. In this study, we propose a plastic scintillator detector which demonstrates the ability to clearly distinguish fast neutrons, thermal neutrons, and gamma rays within mixed radiation fields, offering a practical approach for multi-radiation detection. Two plastic scintillator assemblies: EJ200+EJ426 and EJ276+EJ426 were setup, and the system energy response was calibrated using three  $\gamma$  sources ( $^{137}\text{Cs}$ ,  $^{22}\text{Na}$  and  $^{60}\text{Co}$ ). An Am–Be neutron source was employed, and pulse shape discrimination (PSD) was used to separate fast neutrons, thermal neutrons and  $\gamma$  rays. Using a three-sigma ( $3\sigma$ ) discrimination criterion, the EJ200+EJ426 configuration was found to reliably distinguish thermal neutrons from  $\gamma$  rays, while the EJ276+EJ426 configuration can effectively discriminate fast neutrons, thermal neutrons and  $\gamma$  rays at  $\gamma$ -equivalent energies above 1 MeV.

**KEYWORDS:** Plastic scintillator, Pulse shape discrimination, Neutron, Calibration

ARXIV EPRINT: [1234.56789](https://arxiv.org/abs/2512.15585)

---

## Contents

<b>1</b>	<b>Introduction</b>	<b>1</b>
<b>2</b>	<b>Principle</b>	<b>1</b>
<b>3</b>	<b>Energy calibration</b>	<b>5</b>
<b>4</b>	<b>Pulse shape discrimination</b>	<b>7</b>
<b>5</b>	<b>Fast Neutrons, Thermal Neutrons and <math>\gamma</math> Rays Discrimination Results</b>	<b>8</b>
<b>6</b>	<b>Conclusions</b>	<b>12</b>

---

## 1 Introduction

Particle identification in a mixed radiation field is critical in various scientific and industrial applications, including nuclear safety, radiation monitoring, and high-energy physics experiments [1–4]. In this article, we propose a simple and compact plastic scintillator setup capable of simultaneously distinguishing fast neutrons, thermal neutrons, and  $\gamma$  rays. By improving detection accuracy and reducing operational complexity, this technology has the potential to enhance radiation monitoring systems and contribute to safer environments in nuclear facilities [5].

In this work, we employed three plastic scintillators EJ200 [6], EJ276 [7], and EJ426 [8] for combined detection tests. Signals were acquired using two types of equipment: an oscilloscope and a CAEN DT5751 digitizer[9]. Section 2 provides a detailed description of the plastic scintillators and signal acquisition systems employed in the experiment, along with PMT gain calibration. Section 3 presents energy calibrations for two scintillator combinations—EJ200+EJ426 and EJ276+EJ426—using three  $\gamma$  ray sources. Section 4 and Section 5 systematically investigates particle discrimination among thermal neutrons, fast neutrons, and  $\gamma$  rays using an AmBe neutron source, with measurements performed on three configurations: standalone EJ426, EJ200+EJ426, and EJ276+EJ426.

## 2 Principle

Figure 2 and Figure 1 show a physical photograph of the experimental setup and a schematic diagram of its operating principle, respectively. Signals were acquired using a digital oscilloscope (LeCroy HDO4104A) with a 1 GHz bandwidth and a sampling rate of 10 GS/s. The entire assembly is supported by an external metal frame and enclosed in thick black cloth to form a light-tight box, shielding against ambient light interference. Optical coupling between the scintillator and the PMT was achieved using SL612 optical silicone grease[10] (Beijing Hoton Technology Co.,Ltd.). The

scintillator modules are wrapped with aluminum foil to enhance light sealing and suppress ambient light interference. Lead bricks are placed around the plastic scintillator to reduce the impact of environmental  $\gamma$  background.

The EJ426 scintillator (the EJ426 neutron screen) is thin and fragile, so it is protected by sandwiching it between two transparent polymethyl methacrylate (PMMA) plates. A 6.1cm  $\times$  6.1cm square was removed from the center of a PMMA sheet, facilitating direct coupling between the plastic scintillator and the EJ426 neutron screen. On the opposite side, the PMMA plate is closely attached to layers of high-density polyethylene (HDPE) of varying thicknesses for neutron moderation; this HDPE layer is not used during  $\gamma$  source experiments. The neutron or  $\gamma$  source is positioned on the other side of the setup as required by the experiment.

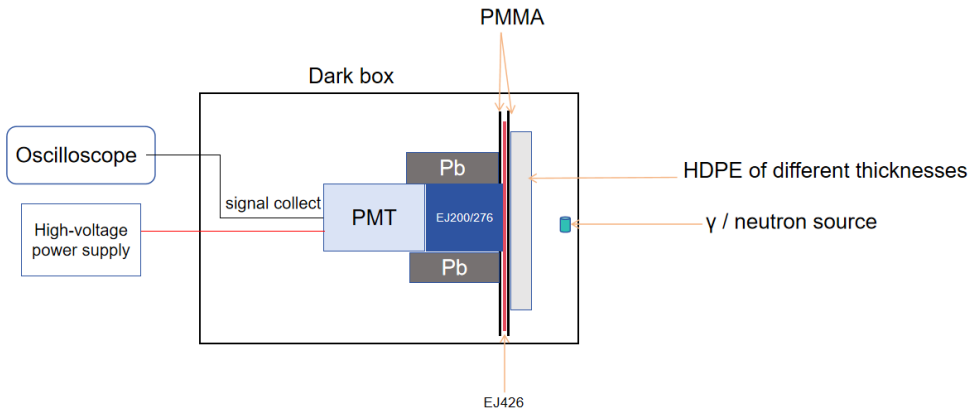


**Figure 1.** Schematic of the experimental setup .The entire experimental setup is enclosed in a dark box. One end of the plastic scintillator is coupled to the PMT via silicone grease, while the other end is coupled to EJ426. The EJ426 is clamped by PMMA and faces the radiation source. When using an Am-Be neutron source, HDPE of varying thicknesses is added as required to moderate neutrons.

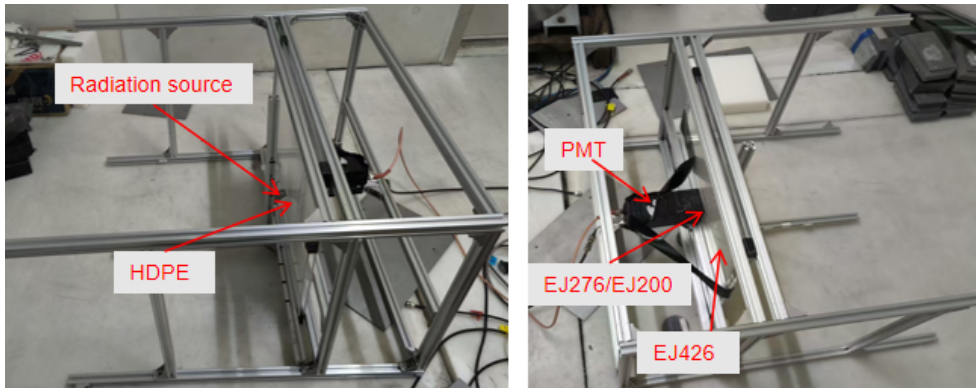


**Figure 2.** The side view(left) and top view(right) of the experimental setup.The PMT is wrapped with black tape and coupled with a plastic scintillator .

The three scintillators used in this experiment are EJ200, EJ426 and EJ276. The basic parameters of the scintillators are summarized in Table 1. Both EJ200 and EJ276 are 6 cm plastic

scintillator cubes, demonstrating good light output efficiency. EJ426 is a  ${}^6\text{Li}/\text{ZnS}(\text{Ag})$  based thermal neutron detection screen with a thickness of 0.32 mm. EJ276 can distinguish between gamma and fast neutrons by their different waveform decay times. The decay time of EJ200 is faster, but it cannot distinguish gamma and fast neutrons. EJ426 is capable of detecting thermal neutrons with a slow decay time while it is not sensitive to  $\gamma$ . EJ426 captures neutrons primarily through the  ${}^6\text{Li}(n, \alpha){}^3\text{H}$  reaction (Equation 2.1), generating  ${}^4\text{He}$  and  ${}^3\text{H}$  ions that subsequently interact with the ZnS scintillator matrix to produce visible photons [11, 12]. The resulting light signals from EJ426 exhibit waveform characteristics compared to the  $\gamma$ -induced signals from the EJ200 plastic scintillator, thereby enabling unambiguous neutron identification. Furthermore, EJ426 demonstrates negligible intrinsic response to  $\gamma$ -rays, making it highly effective for neutron detection in mixed radiation fields.



**Table 1.** The basic parameters of plastics scintillators.<sup>a</sup>

plastic scintillators	Dimensions	Emission Peak (nm)	Decay time(ns)
EJ200	cube 6cm	425	2.1
EJ276	cube 6cm	450	$\gamma:13;35;270 / n:13;59;460^b$
EJ426	Square Sheet 42*0.05cm	450	200

<sup>a</sup>Data from Eljen Technology datasheets [6–8].

<sup>b</sup>Approximate mean decay times of the first three components (ns) for  $\gamma$ /neutron pulses.

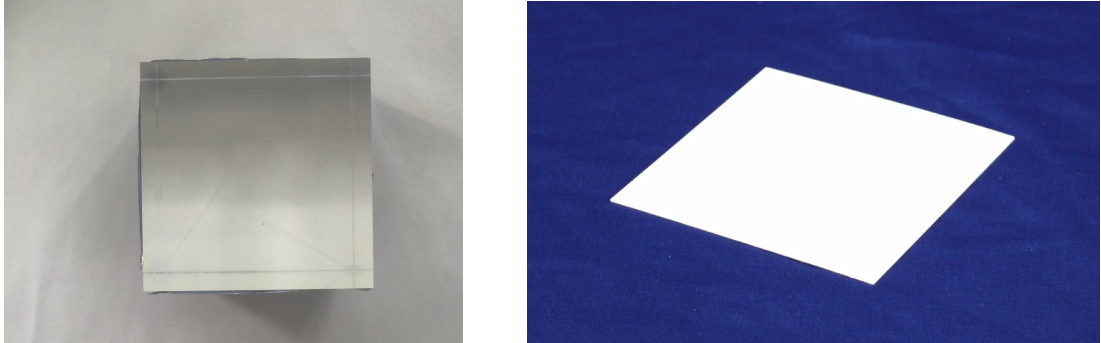


**Figure 3.** Photograph showing the EJ276 (left) and EJ426 (right) [8] scintillators

For this experiment, an XP3232 PMT manufactured by Hainan Zhanchuang Photonics Technology Co.,Ltd. [13] was employed. The XP3232 is a cylindrical vacuum tube with a length of 11.2 cm and a diameter of approximately 5.1 cm. The PMT peak sensitivity at 420 nm, which matches the emission spectrum of the plastic scintillator. Because the PMT diameter is smaller than the side length of the scintillator block, the PMT was coupled directly to the scintillator without additional light guides.

As shown in Figure 4, we have constructed an experimental system for calibrating the gain of a PMT. The setup comprises the following key components: a PMT, a high-voltage power supply,

a signal generator, a single-photon light source based on a laser diode (LD), and a CAEN DT5751 digitizer module (500 MHz bandwidth, 1 GS/s sampling rate), which provides faster read/write performance and integrated timestamp generation compared to the oscilloscope. In the experiment, the signal generator serves a dual purpose: it drives the laser diode to generate single-photoelectron (SPE) signals and simultaneously provides an external trigger to synchronize the acquisition of the PMT output signals by the CAEN DT5751 digitizer. By adjusting the high-voltage power supply, the bias voltage applied to the PMT is precisely controlled, enabling accurate calibration of its gain.

For PMT gain calibration, an appropriate high voltage was first selected. The LD signal pulses were integrated and the integrals were filled into a histogram. The light intensity was then gradually reduced until the fitted peak of the histogram was no longer shifted to the lower values. At that point, the charge spectrum was taken to represent the SPE spectrum.

The charge-integrated spectrum of the SPE signals is shown in Figure 5, which was fitted with a sum of three Gaussian functions: the first peak corresponds to the pedestal, the second to the SPE peak, and the third to the two-photoelectron (2PE) peak.

After determining the operating voltage corresponding to the SPE response, the PMT high voltage was varied stepwise according to a predetermined scheme to establish the voltage–gain relationship, also shown in Figure 5. With the PMT biased at  $-1200$  V, the gain was measured to be approximately  $3.0 \times 10^6$ , and the SPE pulse integral recorded by the oscilloscope was  $24.15$  mV · ns.

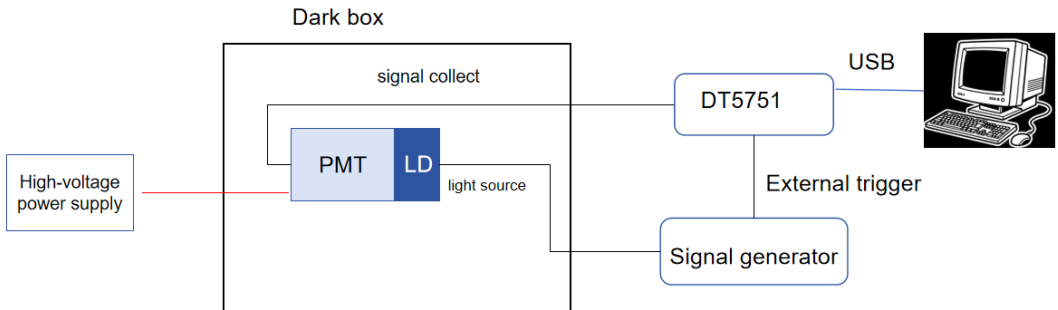


**Figure 4.** Schematic of the PMT gain calibration setup.

Three scintillator combination configurations were employed in this experiment. Energy response calibration and neutron/ $\gamma$  discrimination measurements were performed using four radioactive sources:  $^{137}\text{Cs}$ ,  $^{22}\text{Na}$  and  $^{60}\text{Co}$  ( $\gamma$  sources), and an Am–Be neutron source. The configurations and their respective purposes are as follows:

1. EJ426 + PMT configuration: This arrangement provides the most direct detection of neutron signals. Owing to its high neutron sensitivity, EJ426 allows accurate identification of neutron events through waveform analysis and charge integration of the output pulses.
2. EJ200 + EJ426 + PMT configuration: This hybrid setup enables concurrent measurement of both  $\gamma$ -ray energy deposition and neutron signals. EJ200, a standard plastic scintillator,

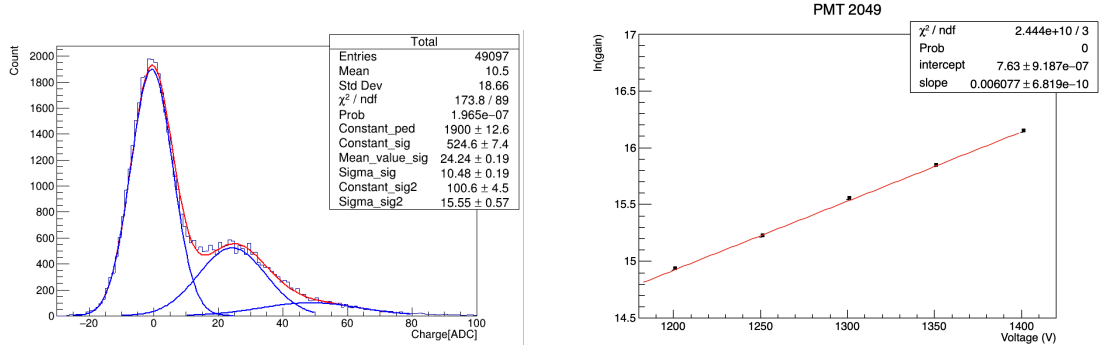


**Figure 5.** Left: The charge-integrated energy spectrum of SPE signals. Right: Relationship between the logarithm of PMT gain and applied voltage.

records  $\gamma$ -ray energy, while EJ426 detects thermal neutrons, allowing comprehensive response characterization in mixed radiation fields.

3. EJ276 + EJ426 + PMT configuration: This setup was primarily used with the Am–Be neutron source to investigate differences in PSD between neutrons and  $\gamma$ -rays. EJ426 is highly sensitive to thermal neutrons, while EJ276 enables simultaneous discrimination of fast neutrons and  $\gamma$ -rays.

The experimental objectives include not only validating the neutron discrimination capability of these scintillator combinations but also performing systematic energy calibration for  $\gamma$ -rays. By leveraging the excellent  $\gamma$ -energy linearity of EJ200 and the neutron sensitivity of EJ426, the overall detector performance in complex radiation environments can be further evaluated.

### 3 Energy calibration

The scintillators used in this study are organic, consisting mainly of carbon and hydrogen, and therefore have relatively low density and effective atomic number; as a result, their  $\gamma$  ray stopping power is limited and they are unlikely to fully absorb the  $\gamma$  rays emitted by the sources. For incident  $\gamma$  rays of approximately 1.5 MeV, interactions in the scintillator are dominated by the photoelectric effect and Compton scattering. Consequently, the energy-response calibration was performed by reconstructing the Compton edge. The  $\gamma$  sources used in this experiment are listed in Table 2.

**Table 2.** Full energy peaks and Compton edge values for Three calibration sources..

$\gamma$ source	$E_{\text{Peak}}(\text{MeV})$	$E_{\text{Compton}}(\text{MeV})$
$^{137}\text{Cs}$	0.662	0.477
$^{22}\text{Na}$	0.511; 1.275	0.341; 1.062
$^{60}\text{Co}$	1.173; 1.333	0.963; 1.118

To obtain the energy spectra of different  $\gamma$  sources for the various plastic scintillator combinations, measurements were performed with an oscilloscope over a 20 minute acquisition period with a threshold set to 40 mV. Signals were recorded both with the source present and with no

source; the net energy-response spectrum was obtained by subtracting the no-source (background) spectrum from the with-source spectrum. The two  $\gamma$  peaks from  $^{60}\text{Co}$  could not be resolved into separate Gaussian peaks because their energies are very close and the limited energy resolution of the plastic scintillator; therefore the mean of the two Compton-edge energies ( $E_{\text{Compton}}$ ) was used for the linear fit. The statistics of the edge resembles the Gaussian fit based on the law of large numbers. The parameter  $\mu$  is obtained by fitting the total integrated oscilloscope signal (in V·ns) corresponding to the Compton-edge energy, as shown in Figure 6.

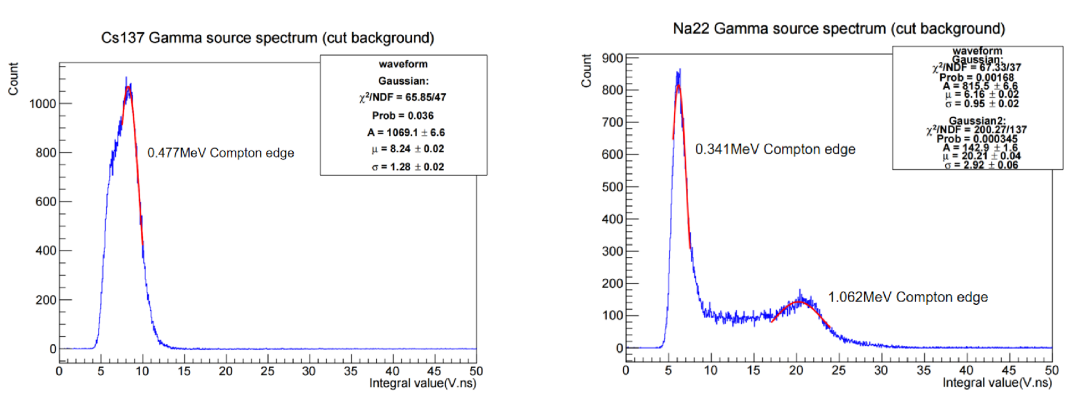


**Figure 6.** Energy spectra measured with a PMT coupled to EJ200+EJ426 and fit of Compton edge. Left: the spectrum of  $^{137}\text{Cs}$  source. Right: the spectrum of  $^{22}\text{Na}$  source.

In Section 2, the signal integral per single SPE was measured. At a PMT bias voltage of  $-1200$  V, this value is  $24.15$  mV · ns. By performing Gaussian fits to the Compton edges of  $^{137}\text{Cs}$ ,  $^{22}\text{Na}$ , and  $^{60}\text{Co}$  sources, the peak positions ( $\mu$ ) and standard deviations ( $\sigma$ ) were obtained. These parameters were then converted into photoelectron (PE) counts using the SPE integral, and a linear fit between PE yield and the corresponding deposited  $\gamma$  energy was performed to determine the light yield for the two scintillator assemblies.

Due to the low density of quenching centers in organic scintillators, the electron energy response remains approximately linear over an energy range of several tens of MeV, allowing reliable extrapolation to other energies.

Figure 7 shows the fitting results: the red data points represent the Gaussian-fit peak positions ( $\mu$ ) of the Compton edges, with error bars indicating the corresponding standard fitting error. The raw signal integrals were converted to PE counts by dividing by the SPE integral (24.15 mV · ns), yielding the detector's light yield for  $\gamma$  rays of different energies. The linear fit is expressed as

$$N_{\text{PE}} = p_0 \cdot E + p_1, \quad (3.1)$$

where  $p_0$  is the light yield (PE/MeV), and  $p_1$  accounts for minor energy losses or baseline offsets during light propagation and detection. The results demonstrate that both plastic scintillator assemblies exhibit a strong linear relationship between light yield and deposited energy over the measured range.

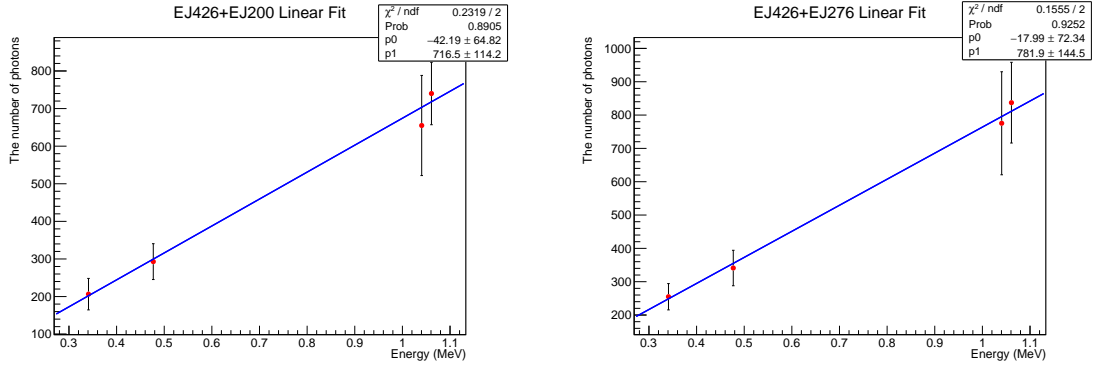


**Figure 7.** Energy linearity of EJ200+EJ426 scintillator detector (left) and EJ276+EJ426 scintillator detector (right), both exhibiting good linearity under calibration with three  $\gamma$  sources.

#### 4 Pulse shape discrimination

Neutron- $\gamma$  rays discrimination is based on the difference in scintillation decay times for neutrons and  $\gamma$  rays in the scintillator. The long-short integration method was employed: neutron and  $\gamma$  signals are distinguished by the ratio of the partial (short) integral  $Q_{\text{short}}$ , to the total (long) integral  $Q_{\text{long}}$ . The PSD value is defined in Equation 4.1 as follows::

$$\text{PSD}_{\text{value}} = 1 - \frac{Q_{\text{short}}}{Q_{\text{long}}} \quad (4.1)$$

As stated in Section 2, the particle discrimination configurations employed in this experiment are PMT + EJ426, PMT + EJ200 + EJ426, and PMT + EJ276 + EJ426. EJ426 was coupled to a PMT and irradiated with a neutron source to study its signal response. As shown in Figure 8, the pulses produced by the EJ426+PMT assembly differ significantly from those generated by EJ200. This distinction arises because EJ426 is a  ${}^6\text{LiF}/\text{ZnS}(\text{Ag})$  composite scintillator: thermal neutrons are captured by  ${}^6\text{Li}$ , producing  ${}^3\text{H}$  and  ${}^4\text{He}$  particles, which then excite the  $\text{ZnS}(\text{Ag})$  phosphor to emit scintillation light [11]. The luminescence decay time of  $\text{ZnS}(\text{Ag})$  is relatively long, resulting in a prolonged pulse duration compared to the fast fluorescence signals produced by ionization from electrons or recoil protons in plastic scintillators. In particular, the pulse widths exhibit markedly different characteristics.

This difference can be exploited for particle discrimination using the ratio of long- to short-gate integrals, as defined in Equation 4.1. A long integration window of 800ns was chosen to capture nearly the entire scintillation pulse, while a short window of 75ns was used to sample the prompt leading edge. As demonstrated in Figure 9, the resulting long/short integral ratio clearly separates the ambient gamma signals from the neutron captures in the setup of PMT+EJ200+EJ426.

This behavior arises because, apart from thermal (slow) neutrons which deposit energy in the EJ426 layer,  $\gamma$  rays do not deposit a significant amount of energy in EJ426. Consequently, the PSD distribution exhibits a clear bifurcation between neutron-induced and  $\gamma$  induced signals. The Figure of Merit (FOM) [14] is defined as

$$\text{FOM} = \frac{|\text{S}_1 - \text{S}_2|}{\text{FWHM}_1 + \text{FWHM}_2} \quad (4.2)$$

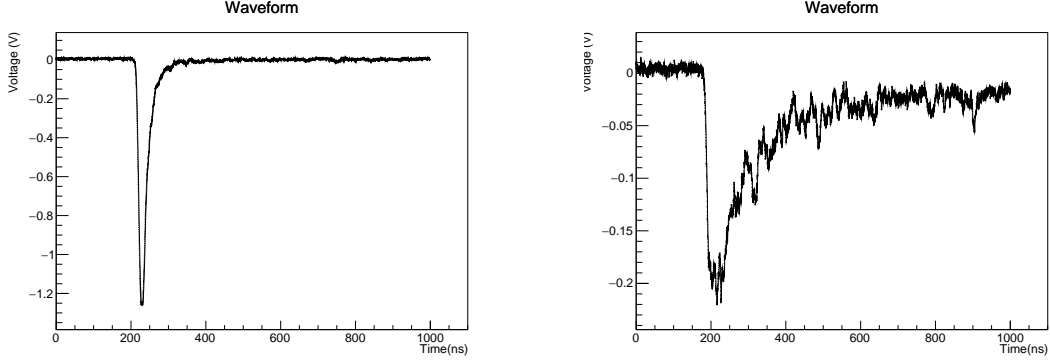


**Figure 8.** Left panel: A single-pulse waveform sample from EJ200 scintillator. Right panel: A single-pulse waveform sample from EJ426 scintillator.

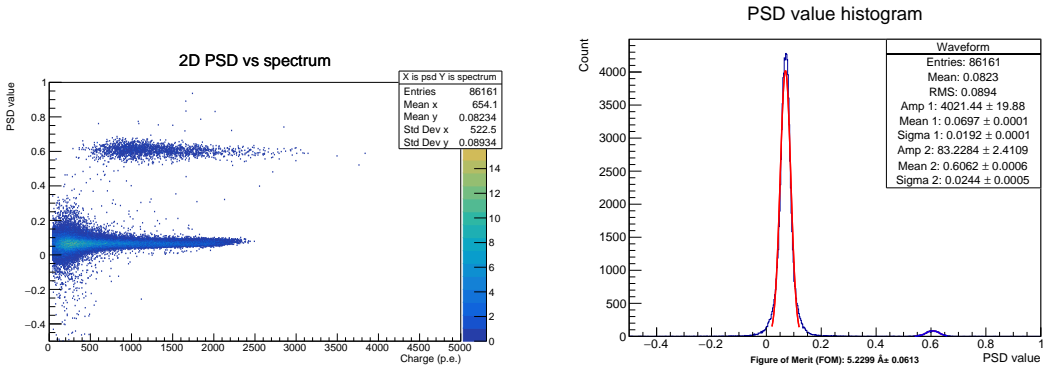


**Figure 9.** Left: 2D histogram of PSD value versus signal charge. The lower peak corresponds to environmental background, while the upper peak represents neutron capture events. Right: 1D histogram of PSD values with Gaussian fits to the two peaks.

where  $S_1$  and  $S_2$  are the mean PSD values for two peaks, respectively, and  $\text{FWHM}_1$  and  $\text{FWHM}_2$  are the corresponding full widths at half maximum. For a Gaussian distribution, the full width at half maximum (FWHM) equals  $2.355$  times the standard deviation  $\sigma$ . A larger FOM indicates better event separation. Thus, a FOM exceeding  $1.27$  corresponds to the two Gaussian peaks being separated by more than three times the sum of their standard deviations, which we take as the criterion for excellent discrimination .

## 5 Fast Neutrons, Thermal Neutrons and $\gamma$ Rays Discrimination Results

In this section, we will introduce the measurements of neutron and gamma discrimination of the two plastic scintillator combinations: EJ200+EJ426 and EJ276+EJ426, by using an Am-Be source. The neutrons were moderated by HDPE slabs of varying thicknesses. Figure 10 shows the PSD distribution for the EJ426+EJ200 assembly, where the horizontal axis represents the energy-calibrated channel number and the vertical axis denotes the PSD value. The signal, expressed in V·ns, is converted to the number of photoelectrons using the PMT gain calibration described in Section 2.

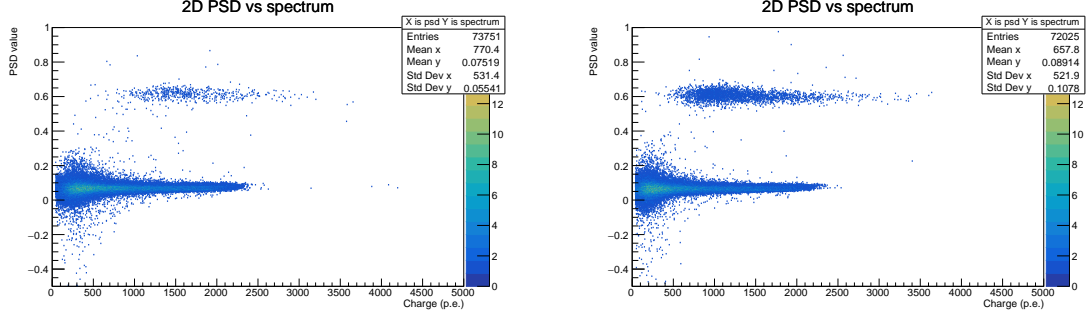


**Figure 10.** Left panel: two-dimensional histogram of PSD value versus the number of PE for the EJ200+EJ426 assembly using an Am-Be source with a 1 cm HDPE moderator. Right panel: corresponding histogram with a 3 cm HDPE moderator. It is evident that increasing the HDPE thickness significantly enhances the thermalization of fast neutrons, thereby increasing the probability of thermal neutron capture reactions in EJ426.

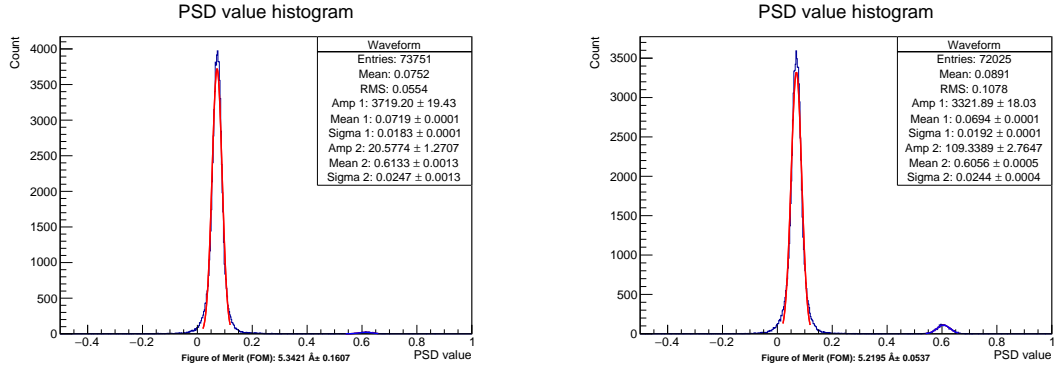


**Figure 11.** Left panel: Gaussian fit of two PSD signal components for the EJ426 coupled to EJ200 with a 1 cm HDPE moderator. The fitted parameters are:  $\mu_1 = 0.0719$ ,  $\mu_2 = 0.6133$ ,  $\sigma_1 = 0.0183$ , and  $\sigma_2 = 0.0247$ . Right panel: Gaussian fit of two PSD signal components for the same detector assembly with a 3 cm HDPE moderator. The fitted parameters are:  $\mu_1 = 0.0694$ ,  $\mu_2 = 0.6056$ ,  $\sigma_1 = 0.0192$ , and  $\sigma_2 = 0.0244$ .

In this configuration, the signals from EJ200 are primarily concentrated in the PSD range of 0–0.2, while the thermal neutron capture events detected by EJ426 appear near PSD  $\approx 0.6$ . We performed independent Gaussian fits to the two signal populations in Figure 11 and obtained a FOM greater than 5. This result demonstrates that the statistical significance of the separation far exceeds the  $5\sigma$  criterion, indicating that the assembly possesses excellent capability for thermal neutron discrimination.

The results show that increasing the HDPE moderator thickness enhances the moderation of fast neutrons, leading to a significant increase in thermal neutron events at PSD  $\approx 0.6$ . In contrast, the event distribution in the PSD range of 0–0.2 remains largely unchanged with increasing HDPE thickness. However, this low-PSD region is dominated by a mixture of  $\gamma$  rays and unmoderated fast neutrons, making it challenging to discriminate fast neutrons and gammas.

Figure 12 presents the PSD measurement for the EJ276+EJ426 detector assembly under irradiation from an Am-Be neutron source. The EJ276 scintillator effectively distinguishes proton

recoil signals induced by fast neutrons from electron ionization signals produced by  $\gamma$  rays, and three well-resolved peaks corresponding to fast neutrons, thermal neutrons, and  $\gamma$  rays are clearly observed:

- The peak at  $\text{PSD} \approx 0.6$  originates from thermal neutron capture events in EJ426 via the  ${}^6\text{Li}(\text{n},\alpha)\text{t}$  reaction;
- The PSD range of 0.16–0.3 corresponds to fast neutron-induced proton recoils in EJ276;
- The region with  $\text{PSD} < 0.16$  is predominantly populated by  $\gamma$ -ray interactions in EJ276.

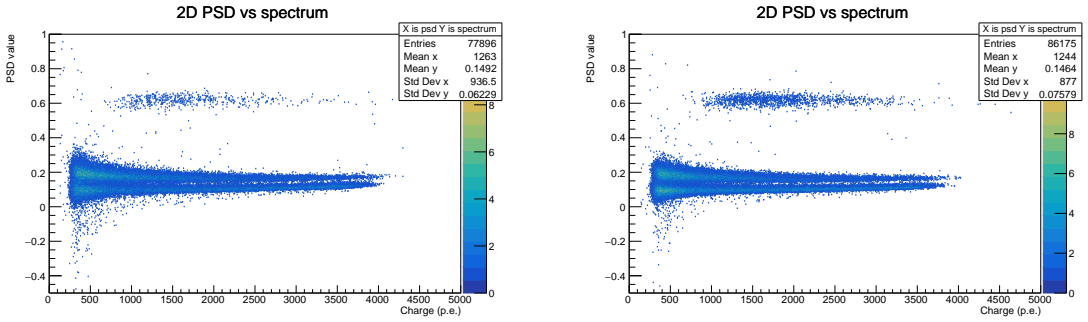


**Figure 12.** Left panel: two-dimensional histogram of PSD value versus the number of PE for the EJ276+EJ426 assembly using an Am-Be source with a 1 cm HDPE moderator. Right panel: corresponding histogram with a 3 cm HDPE moderator.

The PSD distribution was fitted using a sum of three Gaussian functions, and the FOM between each pair of fitted peaks was calculated according to Equation 2.1. The resulting FOM values are shown in Figure 13. The thermal neutron peak from EJ426 is well separated from both the fast neutron and  $\gamma$ -ray peaks of EJ276, with FOM values significantly exceeding 1.27, confirming high-confidence discrimination between thermal neutrons and charged particles/ $\gamma$  rays.

In contrast, the FOM between the fast neutron and  $\gamma$ -ray peaks within EJ276 is 0.96—slightly below 1.27—primarily due to interference from environmental background and baseline drift, which leads to incomplete separation. To evaluate FOM values at different energies, an energy scan with 500 keV window was performed on the 2D PSD distribution. The FOM values obtained with 1 cm, 2 cm, and 3 cm of HDPE are summarized in Figure 14. Using the energy calibration in Section 3, PE number were converted to  $\gamma$  energy. As shown in the figure, for  $\gamma$  energy above 1 MeV the FOM values for fast neutrons and  $\gamma$  rays remain consistently above 1.27. This indicates that the detector configuration is can clearly discriminate gammas with energy above 1 MeV and fast neutrons event.

Table 3 summarizes the event fractions for each particle type under HDPE moderation thicknesses of 1 cm, 2 cm, and 3 cm. As the HDPE thickness increases, the fraction of fast neutron events decreases from 44.91% to 38.99%, while the thermal neutron fraction correspondingly rises from 0.463% to 0.568%. This trend confirms that the polyethylene moderator effectively thermalizes a portion of the incident fast neutrons, thereby validating both the neutron moderation process and the reliability of the particle identification method.

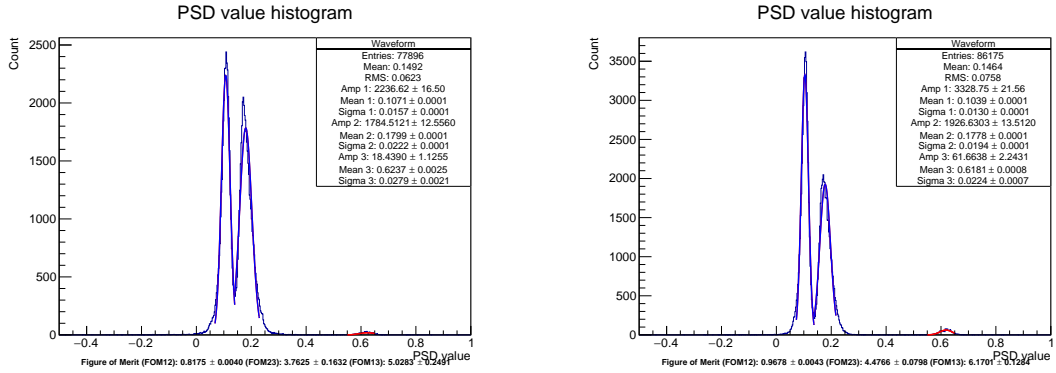


**Figure 13.** Left: Gaussian fit of three PSD signal components for EJ426 coupled to EJ276 with 1cm hdpe. Right : Gaussian fit of three PSD signal components for EJ426 coupled to EJ276 with 3cm hdpe. The values labeled below each plot are the FOM value between each pair of the three Gaussian peaks.

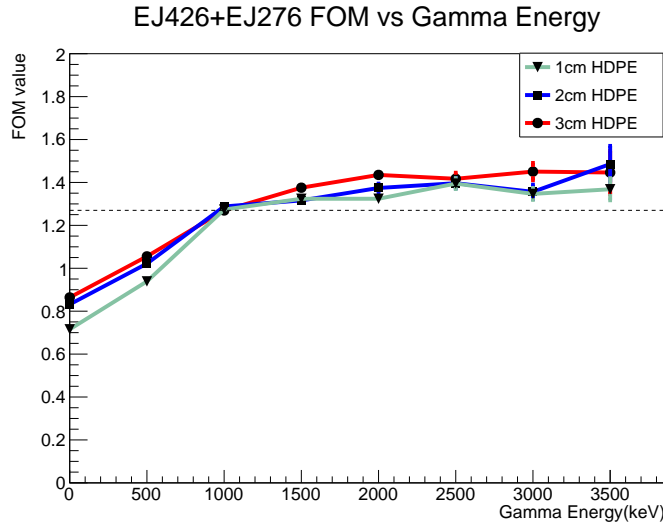


**Figure 14.** FOM values at various  $\gamma$  energy and HDPE moderator thicknesses. The dashed line represents  $\text{FOM} = 1.27$ .

**Table 3.** Event counts, fractions, and totals by particle type for different HDPE thicknesses, acquired in 10 minutes.

HDPE thickness	Thermal neutrons	Fast neutrons	$\gamma$	Total event count
1 cm	674 (0.463%)	65911 (44.91%)	78944 (54.24%)	145529
2 cm	709 (0.540%)	55122 (42.03%)	75311 (57.43%)	131142
3 cm	672 (0.568%)	46135 (38.99%)	71521 (60.44%)	118328

## 6 Conclusions

This study systematically characterizes the energy response and particle discrimination performance of two plastic scintillator configurations: EJ200+EJ426 and EJ276+EJ426. Energy calibration was carried out using three  $\gamma$ -ray sources, establishing a linear energy scale; both configurations exhibit excellent light yield linearity. Particle discrimination performance was further evaluated using an Am–Be neutron source. Coupling EJ200 with EJ426 significantly improved performance, achieving a maximum FOM of 5.34 for thermal neutron/ $\gamma$  discrimination across the entire energy range, with a discrimination significance well above  $5\sigma$ . In contrast, the EJ276+EJ426 configuration enables clear three-way discrimination among fast neutrons, thermal neutrons, and  $\gamma$  rays at  $\gamma$ -equivalent energies above 1 MeV. Specifically, the FOM values for thermal neutron/ $\gamma$  and thermal neutron/fast neutron separation reach 6.12 and 4.39, respectively, over the full energy range; meanwhile, the FOM for fast neutron/ $\gamma$  discrimination exceeds 1.27 above 1 MeV, satisfying the criterion for effective separation. The experimental results demonstrate that both the EJ200+EJ426 and EJ276+EJ426 configurations exhibit strong neutron– $\gamma$  discrimination capability. In particular, with the latter enabling simultaneous identification of fast neutrons, thermal neutrons, and  $\gamma$  rays, which is of great significance for reactor antineutrino experiments and other applications requiring efficient suppression of fast-neutron backgrounds [15–19], and the capabilities of this detector open up significant potential for applications in nuclear safety, radiation monitoring, and high-energy physics, where precise discrimination of different radiation types is essential for accurate measurements and enhanced safety protocols [5, 20, 21].

## Acknowledgments

This research was supported by the China Postdoctoral Science Foundation (Grant No. 2025M783462) and the Fundamental Research Funds for the Central Universities (Grant No. 24qnpj109) and the National Natural Science Foundation of China (Grant No. 12075087). We thank the School of Physics and Institut Franco-Chinois de l’Énergie Nucléaire at Sun Yat-sen University. We are also grateful to Prof. Yuehuan Wei, Prof. Bo Mei, and Prof. Tao Xiong for their support.

## References

- [1] A. Bernstein, N. Bowden, B.L. Goldblum, P. Huber, I. Jovanovic and J. Mattingly, *Colloquium: Neutrino detectors as tools for nuclear security*, *Rev. Mod. Phys.* **92** (2020) 011003.
- [2] O. Akindele et al., *Nu Tools: Exploring Practical Roles for Neutrinos in Nuclear Energy and Security*, [2112.12593](https://arxiv.org/abs/2112.12593).
- [3] R. Carr, J. Coleman, M. Danilov et al., *Neutrino-based tools for nuclear verification and diplomacy in north korea*, *Sci. Glob. Secur.* **27** (2019) 85.
- [4] G.Q. Zhong, K. Li, L.Q. Hu, H.R. Cao, R.J. Zhou, S.Y. Lin et al., *Development of a wide-range neutron flux monitoring system in EAST*, *JINST* **15** (2020) P05011.
- [5] H. Perrey, L. Ros, M. Elfman, U. Bäckström, P. Kristiansson and A. Sjöland, *Evaluation of the in-situ performance of neutron detectors based on EJ-426 scintillator screens for spent fuel characterization*, *Nucl. Instrum. Meth. A* **1020** (2021) 165886.

- [6] Eljen Technology, <https://eljentechnology.com/products/plastic-scintillators/ej-200-ej-204-ej-208-ej-212>(accessed Nov. 28, 2025).
- [7] Eljen Technology,  
<https://eljentechnology.com/products/plastic-scintillators/ej-276>(accessed Nov. 28, 2025).
- [8] Eljen Technology,  
<https://eljentechnology.com/products/neutron-detectors/ej-426>(accessed Nov. 28, 2025).
- [9] CAEN S.p.A., <https://www.caen.it/products/dt5751/1>(accessed Nov. 28, 2025).
- [10] Beijing Haotangxing Nuclear Technology Co., Ltd.,  
<http://www.hoton.com.cn/gxpj/68.html>(accessed Nov. 28, 2025).
- [11] F. Pino, L. Stevanato, D. Cester et al., *Study of the thermal neutron detector zns(ag)/lif response using digital pulse processing*, *JINST* **10** (2015) T08005.
- [12] R. Stedman, *Scintillator for thermal neutrons using  $^6\text{lif}$  and zns(ag)*, *Rev. Sci. Instrum.* **31** (1960) 1013.
- [13] T. Jiang et al., *Study on pulse shape discrimination power of plastic scintillators*, *JINST* **17** (2022) T05002.
- [14] R.A. Winyard, J.E. Lutkin and G.W. McBeth, *Pulse shape discrimination in inorganic and organic scintillators. I*, *Nucl. Instrum. Meth.* **95** (1971) 141.
- [15] NEOS collaboration, *Spectral measurement of electron antineutrinos from a nuclear reactor*, *Phys. Rev. Lett.* **118** (2017) 121802 [[1610.00582](https://arxiv.org/abs/1610.00582)].
- [16] S. Li, *Detection of antineutrinos at the North Anna Nuclear Generating Station*, Ph.D. thesis, Virginia Tech, 2020.
- [17] A. Haghigat, P. Huber, S. Li et al., *Observation of reactor antineutrinos with a rapidly-deployable surface-level detector*, *Phys. Rev. Applied* **13** (2020) 034028.
- [18] G. Luo et al., *Design optimization of plastic scintillators with wavelength-shifting fibers and silicon photomultiplier readouts in the top veto tracker of the juno-tao experiment*, *Nucl. Sci. Tech.* **34** (2023) 99.
- [19] G. Luo et al., *Performance of plastic scintillator modules for top veto tracker at taishan antineutrino observatory*, *Nucl. Sci. Tech.* **36** (2025) 91.
- [20] K.A.A. Gamage and G.C. Taylor, *Neutron gamma fraction imaging: Detection, location and identification of neutron sources*, *Nucl. Instrum. Meth. A* **788** (2015) 9.
- [21] K.A.A. Gamage, A.J. Crompton and M.J. Joyce, *Performance characteristics of a polyethylene collimator with an ej-426 detector in neutron source localisation*, *Nucl. Instrum. Meth. A* **755** (2014) 1.